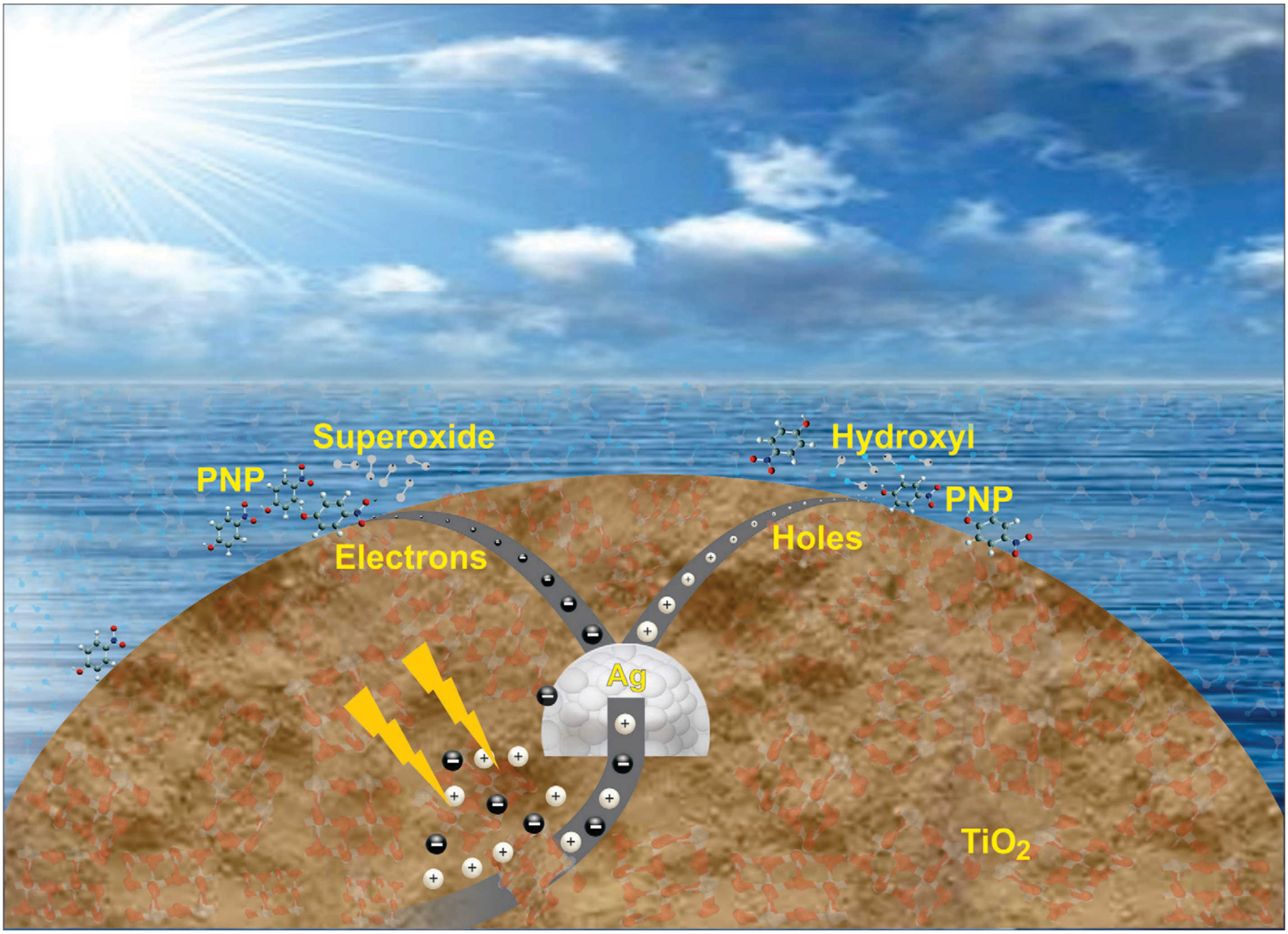

**Showcasing collaborative research from the Department of Physics, University of Mumbai, India & Dipartimento di Fisica, Università degli Studi di Trento, Italy**

Dependence of photocatalysis on charge carrier separation in Ag-doped and decorated $TiO_2$ nanocomposites

Relationships between the photocatalytic efficiency and the contributions of various structures resulting in charge carrier separation, charge transfer and extension of light absorption into the visible range are investigated in the work presented in the above paper. It is shown that for the Ag–$TiO_2$ system the charge separation mechanism is more effective than band-gap reduction or plasmonic effects. The authors propose that for designing the next generation of photocatalysts, more emphasis must be placed on efficient charge carrier separation and efficient charge transfer to the active sites.

## As featured in:

See Ranjana S. Varma *et al.*, *Catal. Sci. Technol.*, 2016, **6**, 8428.

ROYAL SOCIETY OF CHEMISTRY

www.rsc.org/catalysis

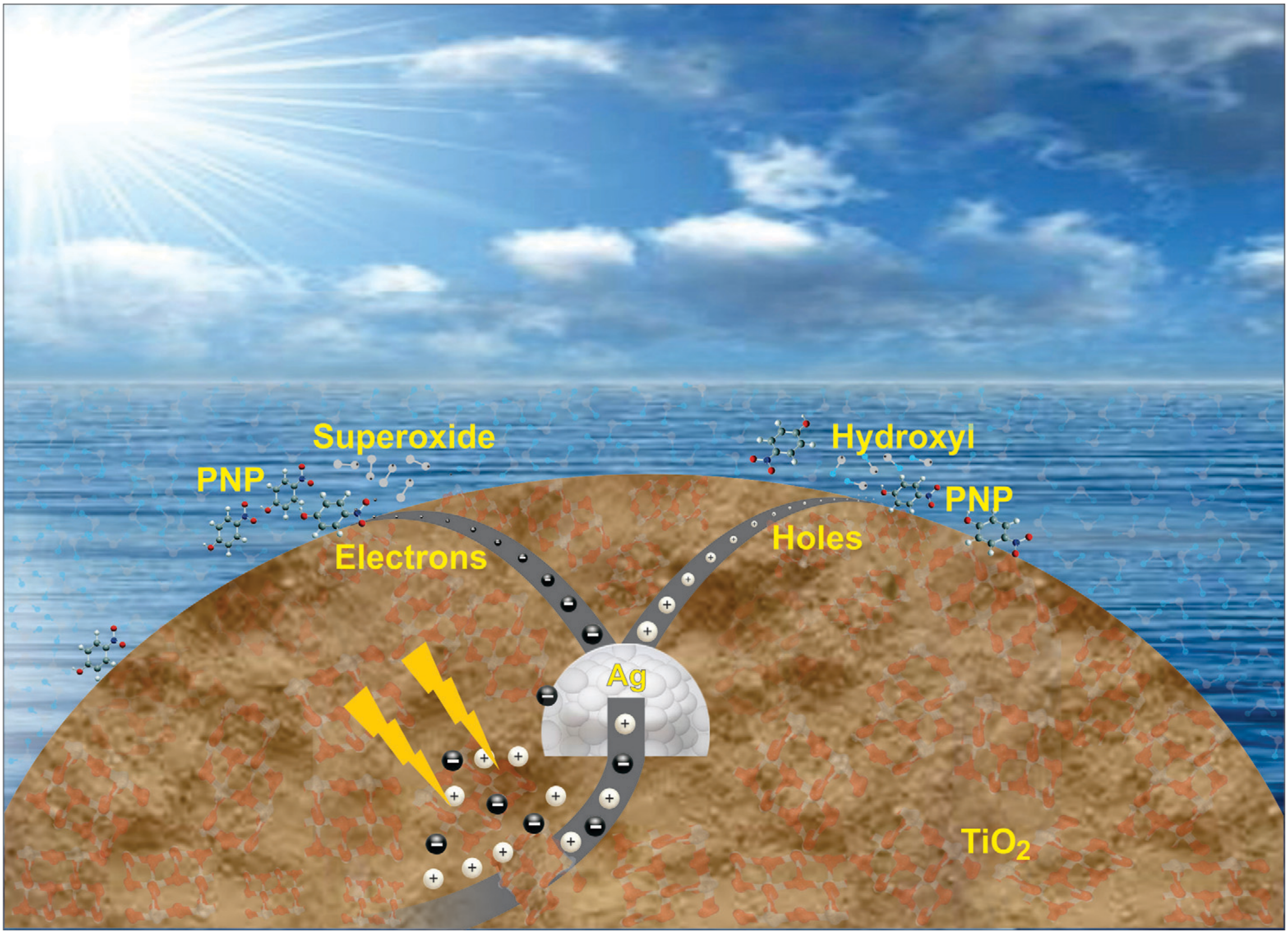

**Showcasing collaborative research from the Department of Physics, University of Mumbai, India & Dipartimento di Fisica, Università degli Studi di Trento, Italy**

Dependence of photocatalysis on charge carrier separation in Ag-doped and decorated $TiO_2$ nanocomposites

Relationships between the photocatalytic efficiency and the contributions of various structures resulting in charge carrier separation, charge transfer and extension of light absorption into the visible range are investigated in the work presented in the above paper. It is shown that for the Ag–$TiO_2$ system the charge separation mechanism is more effective than band-gap reduction or plasmonic effects. The authors propose that for designing the next generation of photocatalysts, more emphasis must be placed on efficient charge carrier separation and efficient charge transfer to the active sites.

## As featured in:

See Ranjana S. Varma *et al.*,
*Catal. Sci. Technol.*, 2016, **6**, 8428.

ROYAL SOCIETY OF CHEMISTRY

www.rsc.org/catalysis

Catalysis Science & Technology

PAPER

View Article Online
View Journal | View Issue

Cite this: *Catal. Sci. Technol.*, 2016, **6**, 8428

# Dependence of photocatalysis on charge carrier separation in Ag-doped and decorated $TiO_2$ nanocomposites†‡

Ranjana S. Varma,*[a] Nirmala Thorat,[a] R. Fernandes,[a] D. C. Kothari,[a] N. Patel[a] and A. Miotello[b]

Received 26th July 2016,
Accepted 15th October 2016

DOI: 10.1039/c6cy01605g

www.rsc.org/catalysis

Two model Ag–$TiO_2$ nanocomposite systems have been investigated with the aim of understanding the relationship between the photocatalytic efficiency and the contributions of various structures resulting in charge carrier separation, charge transfer and extension of light absorption to the visible range. The first model system is based on a composite scheme consisting of $TiO_2$ decorated with Ag nanoparticles (NPs). The second composite scheme consists of $TiO_2$ simultaneously doped and decorated with Ag NPs. Ag–$TiO_2$ nanocomposites containing various concentrations (0.5 to 6 at%) of Ag nanoparticles were prepared, and the photocatalytic degradation of *p*-nitrophenol (PNP) and methylene blue (MB) were investigated. Compared to the Ag-decorated samples, the Ag-doped and decorated samples show enhanced activity due to the synergistic effects of the Schottky barrier, doping and the anatase + brookite mixed phase. It was observed from PL and fluorescence lifetime studies that the charge carrier lifetime correlates with the relative photonic efficiency of the photocatalytic activity. An optimum Ag concentration is required to obtain the maximum lifetime of the photo-generated charges. The photocatalytic activity does not show any correlation to the amount of visible light absorption, to plasmonic effects, or to band-gap reduction. Decorating with silver nanoparticles aids electron transfer and creates electron traps in the form of oxygen vacancies on the surface of $TiO_2$. We show that for the Ag–$TiO_2$ system, the photocatalytic activity is directly proportional to the lifetime of the photogenerated charge carrier.

## 1. Introduction

$TiO_2$ has been widely studied as a photocatalyst to photodegrade many organic pollutants due to its relatively high catalytic activity, physical and chemical stability, and low cost.[1–4] Although there has been much progress in basic research on $TiO_2$, comprehensive applications of $TiO_2$ in the environmental and energy industries are scarce. Among the many drawbacks of $TiO_2$, two of the major ones are its low photocatalytic efficiency and poor visible light absorption. The photocatalytic efficiency mainly depends on the generation and transfer of electrons and holes to the catalytically active sites without recombination for initiating chemical reactions.[5] Therefore, a next-generation photocatalyst material should not only be able to produce more electron hole pairs under visible light but should also simultaneously reduce charge carrier recombination and fast-lane transfer of charges to active surface sites for photocatlytic activity. Many researchers have focused on basic studies to find solutions to these problems;[6–8] for example, by i) band structure engineering to improve the visible light absorption; ii) separation of photogenerated charges by introducing electron/hole traps/sinks; iii) transport of charges to the active surface sites; and iv) synergistic surface plasmon resonance (SPR) effects.

Approaches used by researchers include doping with cations and anions, noble metal loading, and dye sensitization.[6–9] Researchers have demonstrated that the catalytic activity is higher when $TiO_2$ contains a mixture of anatase and brookite phases rather than a single phase due to synergistic mixed-phase effects as well as the robust separation of photoexcited charge carriers between phases.[10] Doping $TiO_2$ is a promising way to extend its light absorption to the visible region, prolong the lifetime of the charge carriers by providing charge carrier trapping sites, and reduce the

---

[a] *Department of Physics and National Centre for Nanosciences & Nanotechnology, University of Mumbai, Vidyanagari, Santacruz (E), Mumbai 400 098, India. E-mail: ranju16@gmail.com; Fax: +91 22 2652 9780; Tel: +91 9821216711*

[b] *Dipartimento di Fisica, Università degli Studi di Trento, I-38123 Povo, Trento, Italy*

† The authors declare no competing financial interests.

‡ Electronic supplementary information (ESI) available: Fig. S1–S7 show photographs of the prepared samples, particle size distributions obtained from TEM images, EDS mapping, XPS survey spectra, lifetime decay fitting, photoactivity degradation of MB dye and Tauc plots for the indirect and direct band gaps for the samples prepared in the present work. Table S1–S3 show the physical properties of the samples. See DOI: 10.1039/c6cy01605g

recombination of photoinduced electrons and holes. Visible photoactivity induced by Ag doping into the lattice of $TiO_2$ has been reported in recent years.[11–13] First principles calculations of the electronic structures of Ag-doped anatase $TiO_2$ suggest that the visible light absorption is due to mixing of the $Ag_{4d}$ states with the $Ti_{3d}$ states in the band gap.[14,15] The experimental results for $TiO_2$ decorated with Ag NPs by photoreduction of $AgNO_3$ on $TiO_2$, as reported by many authors, show an increase in photocatalytic activity.[12–17] In this case, the Schottky barrier formed at the interface of $TiO_2$ and the Ag NPs causes electrons to be transferred to silver thus separating the electron hole pairs. In addition, there are a few reports in which Ag was doped and deposited on $TiO_2$ simultaneously,[18,19] which was more effective than single deposition. However, these studies did not provide any evidence for the roles played by the lifetime of the photogenerated charge carriers in the photoactivity.

The plasmonic effect of metallic nanoparticles has also been exploited to enhance photocatalytic efficiency under visible light irradiation (and, more preferably, under direct sunlight) for environmental and energy applications.[20–22] Plasmonic photocatalysis exploits noble metal nanoparticles attached to semiconductor photocatalysts that cause surface plasmonic resonance (SPR). SPR oscillations can tremendously enhance the local electromagnetic field and can thus be exploited to increase the rate of chemical reactions or for use in surface-enhanced spectroscopy.[22,23] In addition, under visible light irradiation, noble metal nanoparticles act as light harvesters and therefore absorb photons and inject hot electrons ($e_{spr}$) on the surface of the nano-composite system.[24] It is still highly debated whether the electron flows from the semiconductor to the metal due to the Schottky barrier effect or from the metal to the semiconductor due to the SPR effect.[25]

To elucidate the roles played by the lifetime of a photogenerated charge carrier in photoactivity, we have chosen to synthesize nanostructured anatase + brookite mixed phase $TiO_2$ ($ABTiO_2$) decorated with silver nanoparticles, as well as simultaneously decorated and doped Ag–$ABTiO_2$, for the photocatalytic degradation of *p*-nitrophenol (PNP) and methylene blue (MB) under visible light irradiation. The rationale in considering these systems was to understand the relationship between the photocatalytic efficiency and the contributions of various structures resulting in charge carrier separation, charge transfer, extension of light absorption into the visible range and plasmonic effects.

Time-resolved photoluminescence (TRPL)[8] is a promising tool to understand the carrier dynamics of semiconductors in more detail. Because the photoluminescence of semiconductors is a direct result of the charge carrier dynamics, time-resolved photo-luminescence (TRPL) is highly suited for analysis of the phenomena that determine fast charge carrier dynamics in a semiconductor. Analysis was carried out to determine the dependence of the relative photonic efficiency of photocatalytic activity on the lifetime of the charge carriers, the amount of visible light absorption and the band-gap reduction due to Ag doping. We show that for the Ag–$TiO_2$ system, the photocatalytic activity is directly proportional to the photogenerated charge carrier lifetime.

## 2. Experimental section

### Photocatalyst preparation

All the chemicals used were analytical grade reagents and were used without further purification. Double distilled water (DDW) was used in all the experiments. The typical synthesis procedure for mixed phase anatase brookite $TiO_2$ ($ABTiO_2$) NPs is as follows: titanium butoxide [$Ti(OC_4H_9)_4$], ethanol, water and nitric acid ($HNO_3$) were maintained in a molar ratio of 1 : 30 : 15 : 0.1 (for comparison, pure anatase $TiO_2$ ($ATiO_2$) was also prepared). The $TiO_2$ sol was prepared by first stirring $Ti(OC_4H_9)_4$ and ethanol for 1 h, followed by addition of a mixture of water, ethanol and $HNO_3$. The solution was stirred vigorously for 4 h. The resulting solution was allowed to gelate overnight. The gel was then centrifuged, washed with ethanol two times and with water one time, and dried at 70 °C, followed by drying at 120 °C for 2 h to remove excess solvent. Subsequently, the obtained catalyst was crushed into a fine powder and calcinated in a furnace at 450 °C for 2 h. This process was adopted as an optimized method for the preparation of powder $TiO_2$ NPs.

To optimize the amount of silver nanoparticles (Ag NPs) for anchoring and/or doping $ABTiO_2$ nano-composites for high photo-efficiency, different concentrations of Ag–$ABTiO_2$ were synthesized and characterized by spectroscopic methods. Ag ions were decorated on $ABTiO_2$ NPs (prepared by the sol gel method) by an incipient wet impregnation method; $AgNO_3$ was used as the Ag source. To prepare silver ion-loaded $ABTiO_2$ powder samples, 200 mg of $ABTiO_2$ was suspended in 100 ml of $AgNO_3$ solution of the desired concentration (0.5, 1, 2, 6 at%), which was stirred for 4 h for proper mixing. The prepared photocatalyst was washed with water and dried at about 120 °C to eliminate water. Ag ion-loaded $ABTiO_2$ samples were annealed at 450 °C for 2 h for simultaneous doping and the formation of Ag nanoparticles on the surface of $ABTiO_2$ [18] (referred to in the text as DD-$ABTiO_2$, *i.e.* decorated and doped Ag–$ABTiO_2$). $TiO_2$ decorated with Ag NPs was also prepared using the same method but under UV-photoreduction (referred to in the text as D-$ABTiO_2$, *i.e.* decorated Ag–$ABTiO_2$). During the impregnation, Ag nanoparticles were loaded on the $TiO_2$ surface by photoreduction of Ag ions without Ag doping. The solution (200 mg $TiO_2$ + 100 ml $AgNO_3$ of different concentrations) was exposed to UV illumination for 4 h and simultaneously stirred for uniform photoreduction of Ag ions to Ag metal on $TiO_2$ and to ensure that all the silver was photodeposited. The mechanism of Ag nanoparticle formation on the surface of $TiO_2$ by photoreduction has been proposed by Hermann and Sclafani.[26] During the subsequent UV irradiation, the photogenerated electrons reduce the adsorbed $Ag^+$ ions to silver metal atoms. During the photoreduction, the color of the suspension changed from white to grey. After illumination, the samples were repeatedly washed with DDW and then dried. Samples with different Ag contents were tested to determine the optimum composition. The sample nomenclature used in the present work is shown in Table S1,‡ and the colors of the prepared samples are shown in Fig. S1 (in the ESI‡).

### Characterization of samples

To identify the crystalline structure and different phases in the samples, X-ray diffraction (XRD) measurements were performed on a Regaku-Ultima IV powder diffractometer equipped with a Cu $K_\alpha$ source (1.6 kW X-ray tube with applied voltage and current values of 40 kV and 40 mA). Raman spectroscopy was also used to identify various phases. Raman spectra were recorded using a Renishaw micro-Raman spectrometer (RE-04) equipped with a solid state laser with the diode pumped at 514 nm. The morphologies and particle sizes of the samples were investigated by transmission electron microscopy (TEM). TEM, high resolution transmission electron microscopy and selected area electron diffraction (SAED) were performed using a FEG-TEM 300 kV system (Tecnai G2, F30). Energy-dispersive X-ray spectroscopy (EDS) mapping was performed using a FEG-TEM 200 kV system (JEM-2100F). The optical absorption spectra of the samples were measured using a Cary 500 UV-vis-NIR spectrophotometer in diffuse reflectance (DR) mode over the range of 200 to 800 nm against a $BaSO_4$ standard. Brunauer–Emmett–Teller (BET) specific surface area measurements were carried out by determing the $N_2$ adsorption and desorption isotherms on a single point BET surface area system (Smart SORB 93) after degassing all the samples at 120 °C for 2 h. X-ray photoelectron spectroscopy (XPS) (PHI 5000 Versa Probe II) was employed to study the surface atomic compositions and chemical states of the prepared samples. XPS data were obtained using monochromatic aluminum with an Al $K_\alpha$ X-ray source ($h\nu$ = 1486.6 eV) operating at a vacuum of $10^{-7}$ Pa. All the binding energy values were calibrated using the $C_{1s}$ line of 284.8 eV. The recombination rates and lifetimes of the charge carriers in the pure and doped nanoparticles were examined by steady state and time resolved photoluminescence spectroscopy. Steady state photoluminescence (PL) studies were carried out using a fluorescence spectrophotometer (Varian; Cary Eclipse) at two excitation wavelengths (280 nm and 385 nm). Time resolved photoluminescence (TRPL) studies were carried out using the ISS ChronosBH model equipped with a picosecond pulsed (70 ps) laser diode from Hamamatsu with a wavelength of 405 nm and a peak power of 100 mW. Glycogen dispersed in distilled water was used as a scattering sample to measure the instrument response function (IRF). The details of the fitting equations used are given in the ESI.‡ To acquire PL spectra, 3 mg of powder photocatalyst was dispersed in 10 ml of DDW and transferred into a 1 cm × 1 cm quartz cuvette for measurement.

### Measurement of photocatalytic activity

The photocatalytic properties of the as-prepared Ag–ABTiO$_2$ nanocomposite were studied under imitation solar light irradiation (xenon lamp from Hamamatsu, 150 W). The 150 W xenon lamps built into lamp housing with polished anodized aluminum reflectors and placed 47 cm away from the reactor were used. The light flux was measured to be 5 mW cm$^{-2}$ in the reaction solution. For each experiment, 50 mg photocatalyst was dispersed in 50 ml of pollutant (MB or PNP) solution at a concentration of 10 ppm and stirred for 20 min in the dark to attain equilibrium before illumination. Solutions containing the powders were placed in beakers in equal amounts and placed on a magnetic stirrer under a xenon lamp (150 W) so that the illumination was uniform on all the samples. Aliquots were withdrawn at specific time intervals and analyzed. A blank test was also carried out by irradiating the pollutant (PNP or MB) solution without photocatalyst. The photocatalytic activity was determined by measuring the change in the concentration of pollutants using their characteristic absorption bands (320 nm for PNP and 665 nm for MB) obtained on a UV-vis spectrophotometer (Implen Nano Photometer™ Pearl) and plotting the change as a function of irradiation time. The photocatalytic activities of the samples were evaluated by investigating the kinetics of the degradation reactions of the pollutants (PNP and MB) in an aqueous suspension under visible light irradiation. All the experiments were repeated three times to verify the consistency. The best practices for photocatalyst characterization described in references[27,28] were followed. The photocatalytic activity was quantified using the photodegradation rate efficiency determined from the pseudo first order law given by eqn (1),

$$\ln(C(t)/C_o) = -kt, \tag{1}$$

where $C(t)$ is the concentration of the pollutant at any time $t$, $C_o$ is the initial concentration of the pollutant, and $k$ is the photodegradation rate coefficient of the pollutant. The percent degradation (%) has been calculated using eqn (2),

$$\%\text{degradation} = ((A_0 - A_t)/A_0) \times 100 \tag{2}$$

where $A_0$ is the initial absorbance and $A_t$ is the absorbance of the sample irradiated for $t$ minutes. Also, the relative photonic efficiency ($\xi_r$) was calculated based on the model proposed by Serpone *et al.*[29,30] using phenol as a standard organic compound and $TiO_2$ (P-25 Degussa) as a standard photocatalyst (eqn (3)),

$$\xi_r = \frac{\text{rate of organic compound degradation}}{\text{rate of phenol degradation}} \tag{3}$$

## 3. Results and discussion

Two sets of samples were prepared: in the first set, silver NPs were decorated on $TiO_2$ (designated as D-ABTiO$_2$), whereas in the second set, silver NPs were decorated on Ag-doped $TiO_2$ (designated as DD-ABTiO$_2$). Structural characterization of D-ABTiO$_2$ and DD-ABTiO$_2$ was carried out by XRD and Raman spectroscopy; the results are reported in Fig. 1. The XRD patterns show the presence of diffraction peaks due to the anatase and brookite $TiO_2$ phases (Fig. 1(a) and (b)). The inference that silver in decorated form is present on $TiO_2$ is drawn from the XRD patterns of both the set of samples, which display diffraction peaks due to elemental silver (Fig. 1(a) and (b)). Raman spectra also confirmed the presence of anatase and brookite $TiO_2$ phases (Fig. 1(c) and (d)). The intensities of the characteristic Raman peaks of $ABTiO_2$ were observed to increase for both the D-$ABTiO_2$ and DD-$ABTiO_2$ samples with increasing Ag concentration. This increase in intensity is due to the surface-enhanced Raman scattering occurring in the presence of Ag NPs.

Bright field TEM and HRTEM images and SAED patterns of all samples are presented in Fig. 2. As deduced from the peak widths of the XRD patterns (Fig. 1(a) and (b)) and the TEM image (Fig. 2(a)) of the $ABTiO_2$ sample, the sample consists of nanoparticles with a narrow size distribution (7 to 8 nm). The TEM images show that the sizes of the $ABTiO_2$ and D-$ABTiO_2$ nanoparticles are in the same range, while for the DD-$ABTiO_2$ sample, the average size increases (from 7–8 nm to 7–9 nm) (Fig. 2(a), (d) and (g) and Fig. S2 in ESI‡), which was also confirmed from the XRD analysis. The HRTEM image shows a composite grain of anatase and brookite phases (Fig. 2(c)). The presence of a lattice interplanar spacing of 0.35 nm, corresponding to the (101) plane of anatase phase, together with the interplanar spacing of 0.29 nm, corresponding to the brookite (121) plane, reveals the mixed-phase nature of $TiO_2$. The region indicated by an arrow in Fig. 2(c) shows the overlapping of anatase and brookite crystallites and the interface between them. The lattice spacing of the anatase (101) plane matches that of the brookite (210) plane (0.35 nm) in the region where the two crystallites overlap. Thus, the $ABTiO_2$ powder consists of a composite of two phases, originating from anatase and brookite $TiO_2$, and not a mere physical blend of two different particles with two phases. The HRTEM image of the $ABTiO_2$ sample shows lattice fringes with an interplanar spacing of 0.24 nm, corresponding to the Ag (111) plane (Fig. 2(f)). The HRTEM image of the DD-$ABTiO_2$ sample shows that the lattice spacing expands and displays considerable waviness, as indicated by the arrow in Fig. 2(i). These defects are due to stress that exists because of the oversized doped silver ions. There is no noticeable change in the nanocrystal lattice spacing value corresponding to the anatase (101) plane for D-$ABTiO_2$ samples (containing only decorated Ag but without

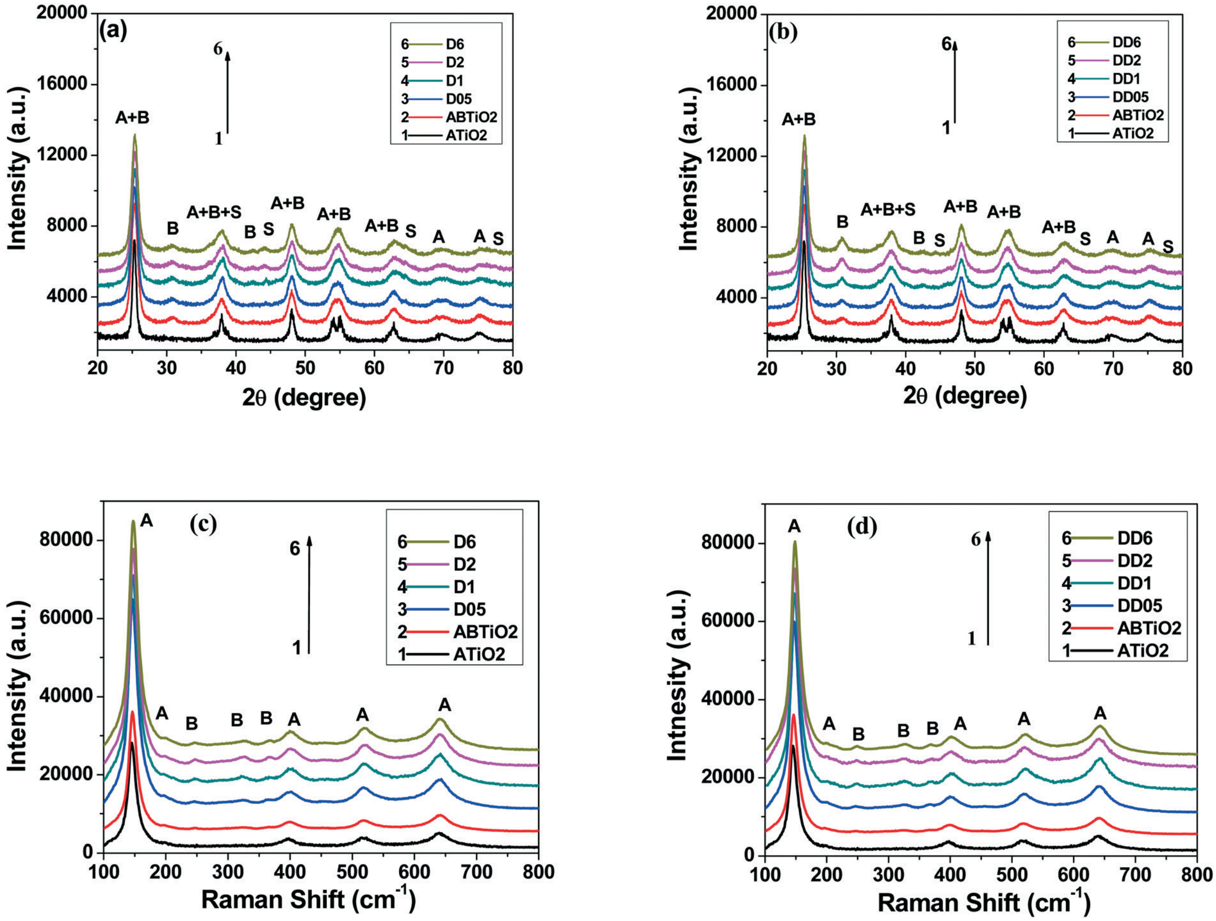

**Fig. 1** XRD patterns and Raman spectra of (a and c) $ATiO_2$, $ABTiO_2$, D-$ABTiO_2$ powders with different silver concentrations; (b and d) $ATiO_2$, $ABTiO_2$, DD-$ABTiO_2$ powders with different silver concentrations.

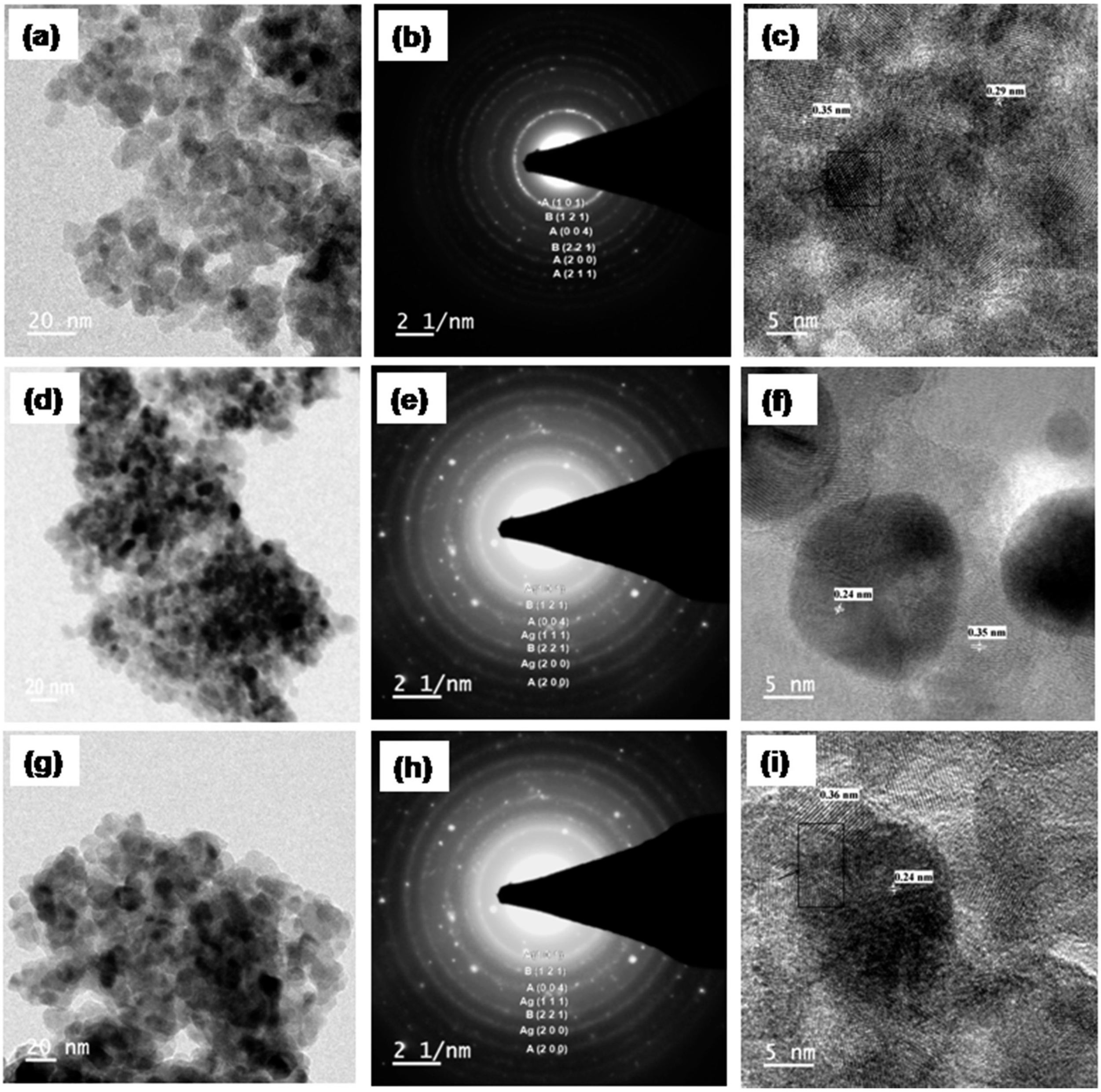

**Fig. 2** TEM images, SAED patterns and HRTEM images of (a–c) ABTiO$_2$, (d–f) D-ABTiO$_2$, (g–i) DD-ABTiO$_2$ powders for 1 at% Ag.

Ag doping in the TiO$_2$ lattice), as seen in Fig. 2(f). Further observation by SAED during TEM imaging (Fig. 2(b), (e) and (h)) confirmed that the nanoparticles have a polycrystalline structure. The HRTEM results and the SAED patterns are in accordance with the XRD results. Perfect agreement in the *d* values calculated from the experimental diffraction ring patterns and literature data is evident. An EDS mapping analysis of the Ag-decorated and doped TiO$_2$ sample (DD1) also confirmed that the prepared nanoparticles, composed of elemental Ag, are dispersed on the surface of the TiO$_2$ nanoparticles with Ti and O signals (Fig. S3 in the ESI‡). Thus, the Ag–ABTiO$_2$ nanocomposite is confirmed by TEM and HRTEM analysis to have a polycrystalline structure, which is an essential characteristic for a good photocatalytic material.

XPS was performed to study the surface layer elemental compositions and the chemical states of the different TiO$_2$ samples. Fig. S4 (ESI‡) shows the comparison of survey spectra of ATiO$_2$, ABTiO$_2$, D-ABTiO$_2$, DD-ABTiO$_2$ (1 at% Ag) samples. As seen from the survey spectra, all the samples show characteristic peaks of Ti and O, while the D-ABTiO$_2$ and DD-ABTiO$_2$ samples show an extra peak around 464.0 eV, assigned to Ag. The narrow scan of Ti 2p is presented in Fig. 3(a); two peaks are observed at the binding energies of 464.0 eV and 558.4 eV, attributed to Ti 2p$_{1/2}$ and Ti 2p$_{3/2}$, respectively, corresponding to Ti$^{4+}$ species. A small signal of Ti$^{3+}$ species in the Ti 2p$_{3/2}$ level is also detected as a shoulder at 456.5 eV. The relative intensity of the two contributions are 91.9% (Ti$^{4+}$) and 8.1% (Ti$^{3+}$) for ABTiO$_2$ sample synthesized in the present work. $Ti^{3+}$ has been suggested to be important to enable facile transfer of an electron or hole and is beneficial for enhancing photoactivity compared with $ATiO_2$.[31] Furthermore, Fig. 3(a) shows that the Ti 2p peaks shift to higher binding energies after decoration or doping with Ag nanoparticles. The observed small shift due to the presence of Ag NPs on the surface of $ABTiO_2$ can be attributed to the electron transfer from $TiO_2$ to Ag due to metal–semiconductor contact.[20,21] For the DD-$ABTiO_2$ sample, the positive shift in binding energy of 0.22 eV compared to that of pure $TiO_2$ signifies that silver is present in the $TiO_2$ lattice and influences the local chemical states of $Ti^{4+}$ ion. The peak at 456.54 eV due to $Ti^{3+}$ is significantly suppressed in D-$ABTiO_2$ and vanishes for DD-$ABTiO_2$.

Fig. 3(b) shows the O1s photoelectron peak of $ABTiO_2$, which can be deconvoluted into two components at 530.9 eV and 529.7 eV. The former can be attributed to absorbed hydroxyl groups, while the latter can be attributed to the lattice oxygen of $TiO_2$, with contributions of 20.1% and 79.9%, respectively. For the D-$ABTiO_2$ and DD-$ABTiO_2$ samples, the hydroxyl oxygen content was found to slightly increase. XPS analysis also reveals the presence of elemental silver in both samples (Fig. 3(c) and (d)), with two peaks centered at 367.5 eV and 373.5 eV for Ag $3d_{5/2}$ and Ag $3d_{3/2}$, respectively. In simultaneously doped and decorated Ag–$TiO_2$ (DD-$ABTiO_2$ sample), evidence of the doped Ag can be seen by XPS (Fig. 3(d)) and HRTEM (Fig. 2(i)). In the XPS spectrum, shown in Fig. 3(d), the Ag$3d_{5/2}$ and Ag $3d_{3/2}$ deconvoluted peaks seen at 366.6 eV and 372.5 eV are due to $Ag^+$ ions, which are incorporated in the $TiO_2$ lattice by substitutionally replacing $Ti^{4+}$ ions and forming Ti–O–Ag bonds.[19] No such peaks are observed for the D-$ABTiO_2$ sample (observed (Fig. 3(d)).

High visible light absorption due to plasmonic effects and a small shift towards the visible light region in the doped samples are observed in the UV-visible absorption spectra. Fig. 4(a and b) show the UV-visible absorption spectra of D-$ABTiO_2$ and DD-$ABTiO_2$ for different silver concentrations. The observed high absorption below 370 nm is usually ascribed to charge transfer from the valence band (mainly formed by the 2p orbitals of the oxide anions) to the conduction band (mainly formed by the $3d_{t2g}$ orbitals of the $Ti^{4+}$ cations).[32] Generally, metallic nanostructures are characterized by their strong interactions with resonant photons through the excitation of surface plasmon resonance (SPR). SPR is

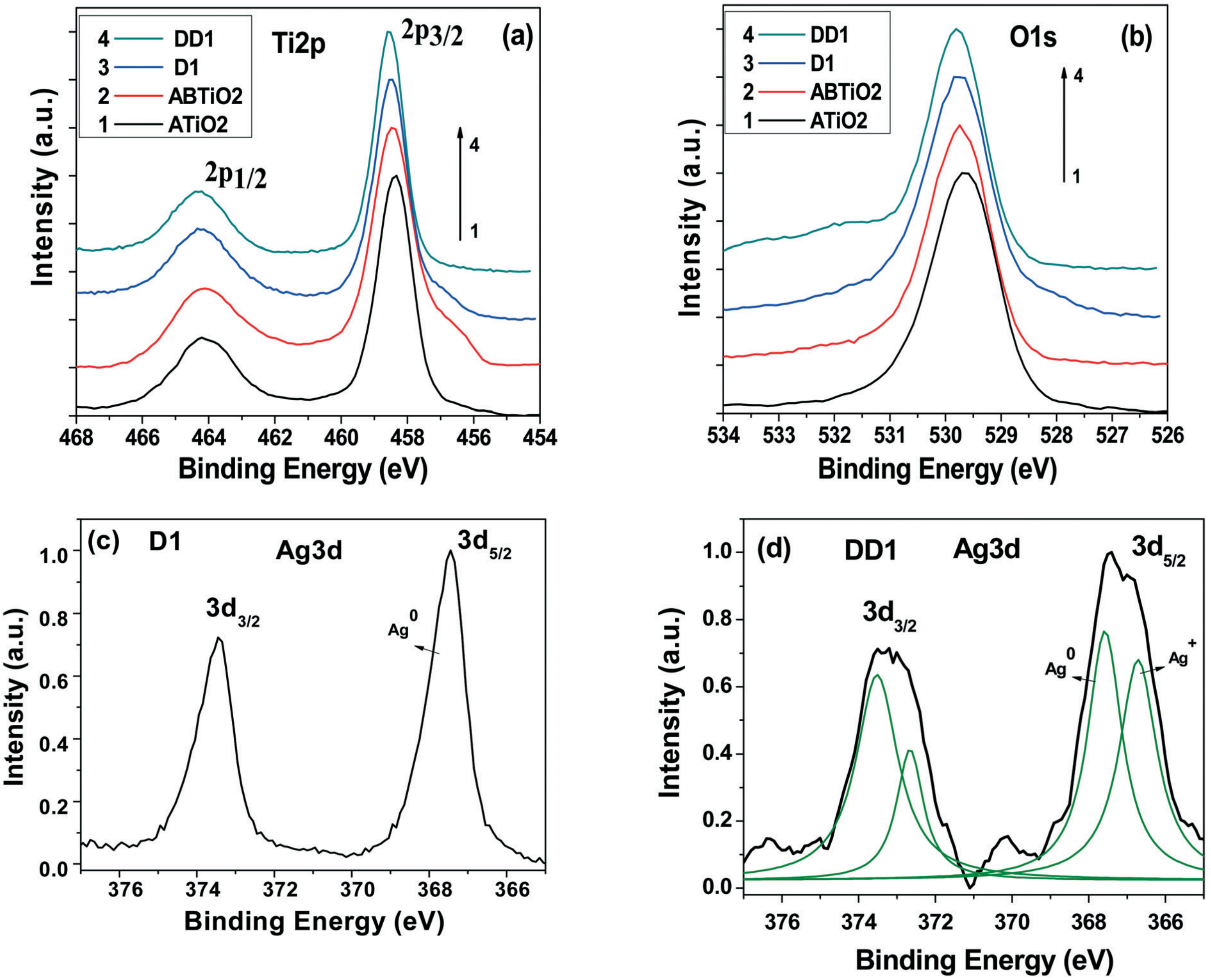

**Fig. 3** XPS spectra of (a) Ti 2p, (b) O 1s of $ABTiO_2$, $DABTiO_2$, $DDABTiO_2$, and (c), (d) Ag 3d levels of the $DABTiO_2$ and $DDABTiO_2$ (1 at% Ag) samples.

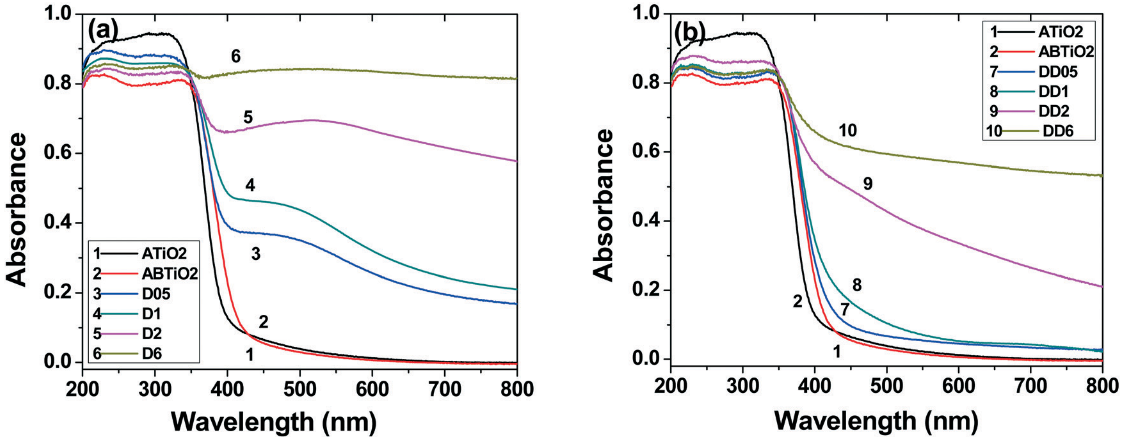

**Fig. 4** (a and b) UV-vis absorption spectra of the D-ABTiO$_2$ and DD-ABTiO$_2$ samples.

characterized by a build-up of intense, spatially non-homogeneous oscillating electric fields in the neighborhood of the nanostructure. In our case, the addition of silver ions by the impregnation method and subsequent annealing or UV irradiation causes significant changes to the absorption spectrum, resulting in high absorbance in the visible region, which is characteristic of surface plasmon absorption. The resonant wavelength and SPR intensity depends not only on the nature of the metal, but also on the size and shape of the metallic nanostructures.[33] The observed band in the visible region is characteristic of Ag surface plasmon absorption. The effects of SPR can also be seen in the Raman spectra (Fig. 1(c and d)). Further, the Ag ion doping was found to introduce an isolated Ag 4d energy level above the VBM of TiO$_2$, favoring the absorption of visible light,[20] which exhibits a slight shift in the band-edge in the absorption spectrum of the doped and decorated sample (clearly seen in curves 7 and 8 in Fig. 4(b); for the other curves, 9 and 10, the large contribution from SPR masks the shift). The specific surface areas of the ABTiO$_2$ particles before and after surface modification were determined using the BET nitrogen gas adsorption method. The specific surface areas obtained are shown in Table S1 (ESI‡). It is observed that the specific surface area decreases with increasing silver content in the Ag–TiO$_2$ catalyst. The decrease in the specific surface area of the doped and decorated TiO$_2$ sample likely occurs because the higher number of decorated particles on the surface increases the overall size compared to the undecorated sample. Generally, the photocatalytic reaction occurs by the absorption of O$_2$ and H$_2$O on the surface of the photocatalyst, which generates oxidizing agents in the form of electrons and holes, respectively. Thus, the decrease in specific surface area may lead to a decrease in photoactivity with increasing Ag concentration; this is not observed, as shown later.

The PL spectra for the Ag–TiO$_2$ nanocomposite samples after band gap excitation (385 nm) are shown in Fig. 5(a and b). The spectra show three main emission peaks at 424 nm (2.92 eV), 486 nm (2.55 eV) and 525 nm (2.36 eV). The PL emission spectrum is an important tool to study the efficiency of charge carrier trapping, transport and transfer. The PL spectrum of TiO$_2$ is related to the recombination of photoinduced electrons and holes, free excitons and self-trapped excitons (STE); these may result from surface defects in the nanosized TiO$_2$ crystals, such as lattice distortion and surface oxygen deficiencies.[32] On the basis of the transition energy diagrams of TiO$_2$ particles calculated by Daude *et al.*,[34] the first two higher energy bands are attributed to shallow traps, while the third energy band is attributed to deep surface states near the Ti$^{4+}$–OH surface. The deep trap levels identified with oxygen vacancies are established at energies from 0.7 to 0.8 eV below the CB. The emission peak at 424 nm is assigned to self-trapped excitons (STE) localized on TiO$_6$ octahedra.[35] After photoexcitation at 385 nm, the electrons in the conduction band move through the ionic lattice, interact with the lattice ions and then localize on a lattice site. The localized electron captures a hole and generates self-trapped excitons.[35] The localization of the STE depends on the length and compactness of the chain of TiO$_6$ octahedra. The peak at 486 nm is attributed to the charge transfer from Ti$^{3+}$ to oxygen anion in a TiO$_6$ octahedral complex associated with oxygen vacancies at the surface, indicating that the band is originating from the intrinsic state rather than from the surface state.[35] Therefore, the 486 nm band can be assigned to self-trapped excitons localized on octahedral TiO$_6$. The quenching of the self-trapped excitonic peak is due to the interaction of the excitons with lattice defects, dopants, *etc.* These interactions collapse the STE to a free electron and hole, thus reducing the emission efficiency. The emission intensity of the Ag–ABTiO$_2$ nanocomposite is lower than that of ABTiO$_2$ and the ATiO$_2$ NPs, suggesting that the recombination of photogenerated electrons and holes is effectively suppressed. When the decorating amount of Ag is relatively small, the recombination of photo-generated electron–hole pairs is suppressed, whereas with higher loading of silver, the suppression ability decreases (Fig. 5(a and b)). Therefore, there is an optimal loading

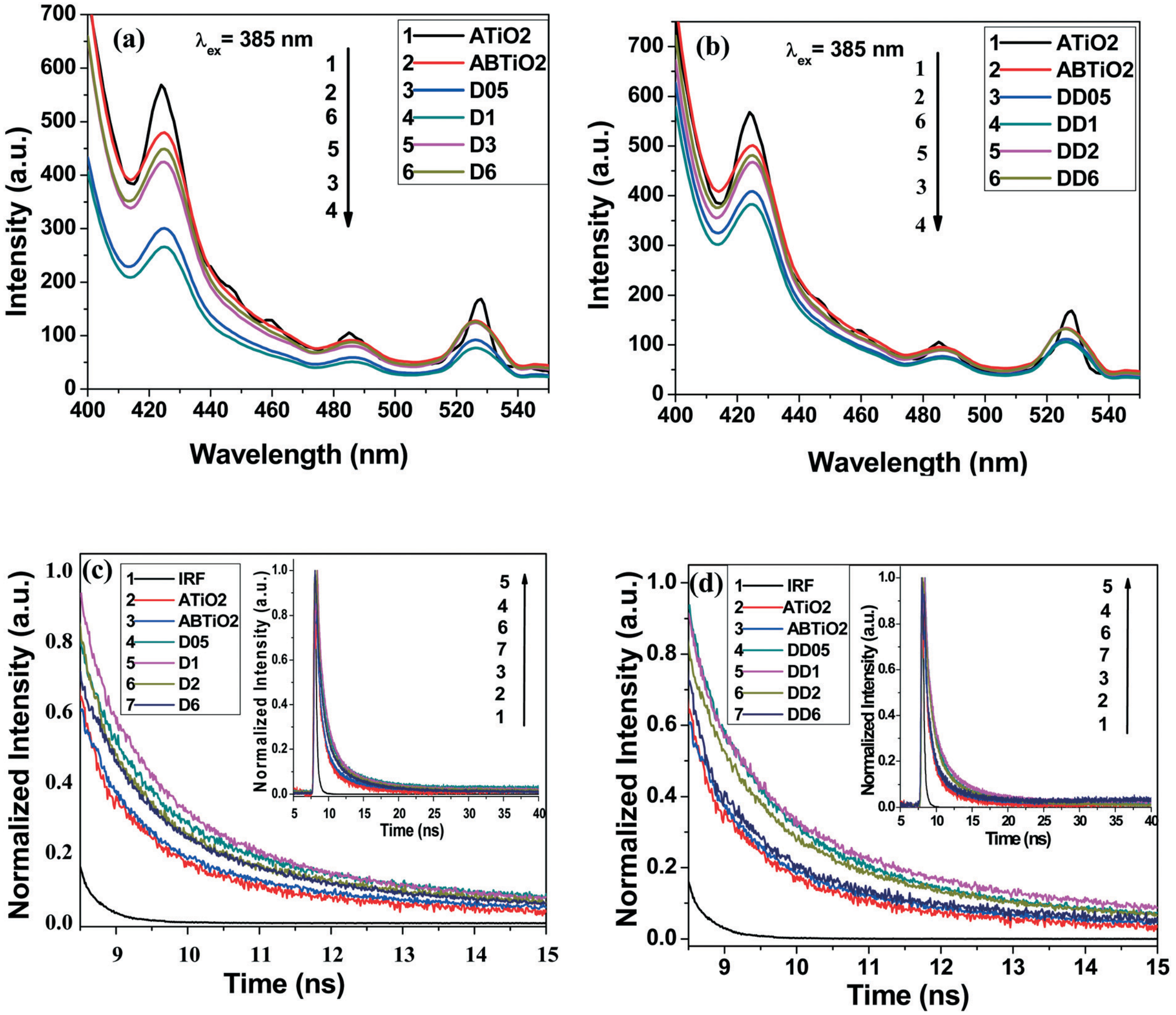

**Fig. 5** PL and TRPL spectra of (a and c) D-ABTiO$_2$ powder and (b and d) DD-ABTiO$_2$ powder with different silver concentrations (inset of TRPL shows the complete decay curve for reference).

amount. It can be observed that the lowest recombination rate is obtained for 1 at% Ag. This result conforms with the TRPL data, as follows.

TRPL measurements were performed to validate the steady-state measurements and quantify the relevant time scales for quenching. To understand the recombination dynamics of the photogenerated charge carriers, the PL decay times were measured by exciting the samples with a 405 nm pulsed diode laser near the band gap energy. Fig. 5(c and d) show the TRPL spectra of three different surface emissions (424, 486 and 525 nm), as observed in the PL spectra after band edge excitation for all samples, which were acquired after pulsed laser (ps) excitation at a wavelength of 405 nm at room temperature. Following electron–hole pair formation and subsequent charge carrier separation, in competition with recombination, a fraction of the electrons and holes are trapped at lattice sites (oxygen vacancies and other defects) or surface states. Some electrons and holes migrate to the surface, where they are trapped at various sites to give Ti$^{3+}$ centers (deeply trapped electrons in Ti$^{4+}$ sites). The multi-exponential decay behavior, characterized by three relevant times, namely $\tau_1$, $\tau_2$, and $\tau_3$ as discussed below, is considered to be due to the distribution of shallow and deep trapping sites inside the TiO$_2$ nanoparticles. The fitting of the three lifetime components is also shown for the reference in Fig. S5 (ESI‡). The incoming photon, with an energy of 3.06 eV (405 nm), results in the formation of a free electron and a hole in the conduction band and valence band, respectively. Some of the photogenerated charge carriers quickly recombine radiatively in the band edge and give rise to the near band edge emission of TiO$_2$. The fast component, $\tau_1$, may be due to the near band edge relaxation of TiO$_2$. Some other photogenerated charge carriers relax to the shallow-trap levels, which radiatively recombine with the lifetime of $\tau_2$. The remaining photogenerated charge carriers can relax to the deep-trap levels and consequently recombine radiatively with a much longer lifetime, $\tau_3$. The slower decay times of the deep-trap emission suggest that the charge-carrier recombination is significantly prolonged in the deep-trap surface state of $TiO_2$. The average lifetimes and the related% fraction and amplitudes of the corresponding decays are given in Table S2 (in ESI‡). The fast decay time (0.17 ns) (34.3%) with an almost similar fraction of two slower decay components (1.05 and 3.85 ns) (31.1 and 34.6%) is observed for $ABTiO_2$. It may be seen from Table S2 (ESI‡) that the fast component, $\tau_1$, and the slowest component, $\tau_3$, initially increase and later decrease as the silver concentration increases for both sets of samples. The average lifetime $\tau$, calculated for the three components, also shows a similar trend, as seen in Table S2 (ESI‡) and Fig. 7(a and b). Fig. 7(a and b) also show the relative photonic efficiency of photocatalytic activity calculated from Fig. 6, which clearly correlates with the average lifetime $\tau$.

The photocatalytic activities of all the prepared samples were tested by examining the degradation of organic pollutants (PNP) as a function of time (Fig. 6(a and b)). The decreases in the relative concentrations of PNPs were estimated by measuring the relative intensity of the peak at 320 nm from the optical absorbance spectra. The photocatalytic activities of the $ATiO_2$, $ABTiO_2$, D-$ABTiO_2$ and DD-$ABTiO_2$ samples were tested by examining the degradation of PNP as a function of time, which is also shown in Fig. 6(a and b). Fig. 6(c and d) shows the percentage degradation of PNP with and without photocatalyst for both samples (D-$ABTiO_2$ and DD-$ABTiO_2$). It was observed that the degradation of PNP was most efficient for 1 at% silver in the $ABTiO_2$ catalyst. The apparent rate constants and relative photonic efficiencies were calculated using eqn (1) and (3) and are summarized in Table S3 (ESI‡). It can be seen that decorating $ABTiO_2$ or simultaneously decorating and doping it with silver favors the removal of organic pollutants such as PNP, as investigated in the present work. However, the activity of the photocatalysts for the removal yield of organic pollutants initially increases with increasing doping concentration and reaches a maximum for a level of 1 at% Ag. The relative photonic efficiency was found to be 3.15 for PNP. As the Ag concentration increases further, the efficiencies decrease, indicating that an optimum concentration of dopant is required. As a reference, the photocatalytic activities of all the prepared samples for

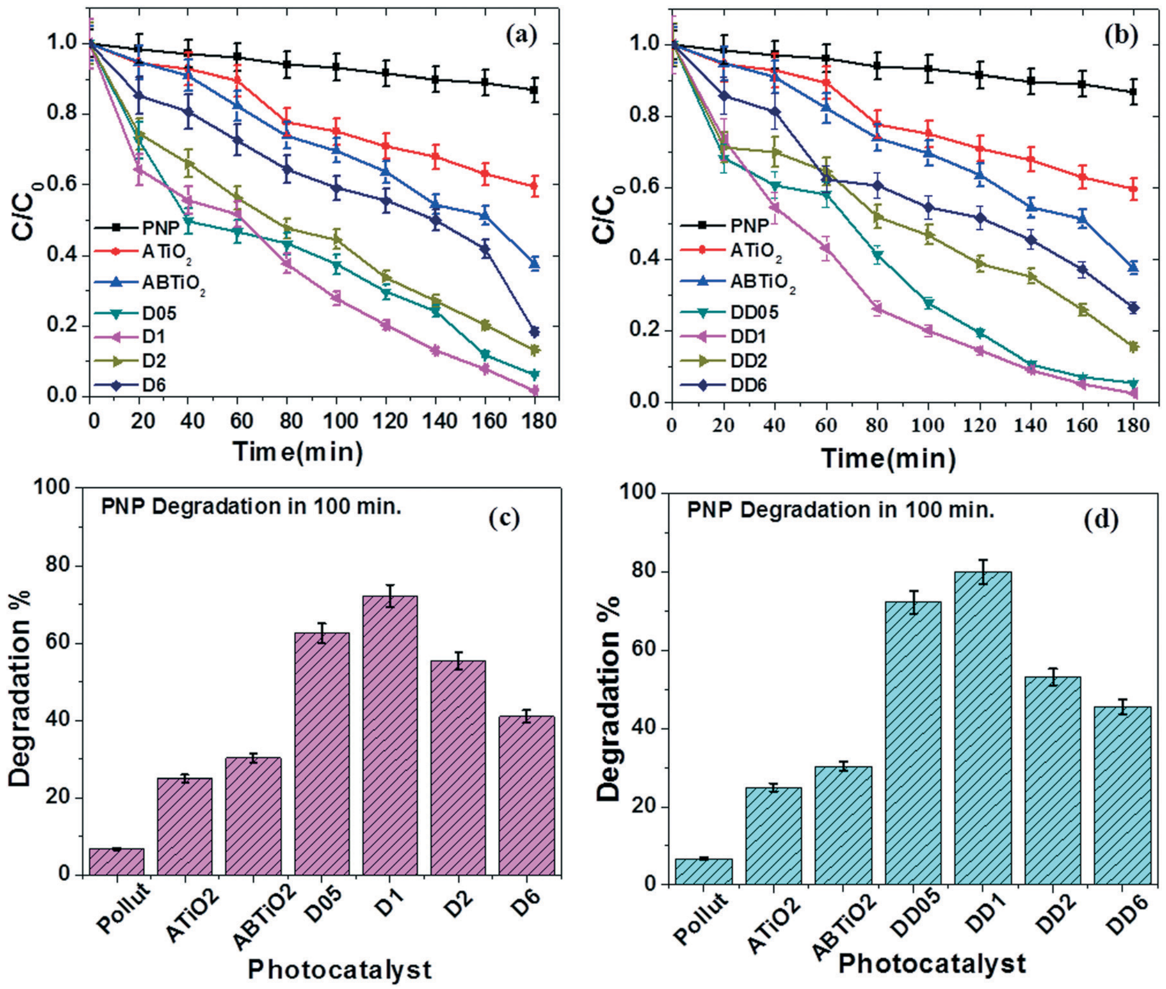

**Fig. 6** (a and b) Comparison of the photocatalytic degradation of organic pollutants (PNP) under light irradiation for D-$ABTiO_2$ and DD-$ABTiO_2$; (c and d) percentages of degradation of the PNP phenol group at 120 min for D-$ABTiO_2$ and DD-$ABTiO_2$.

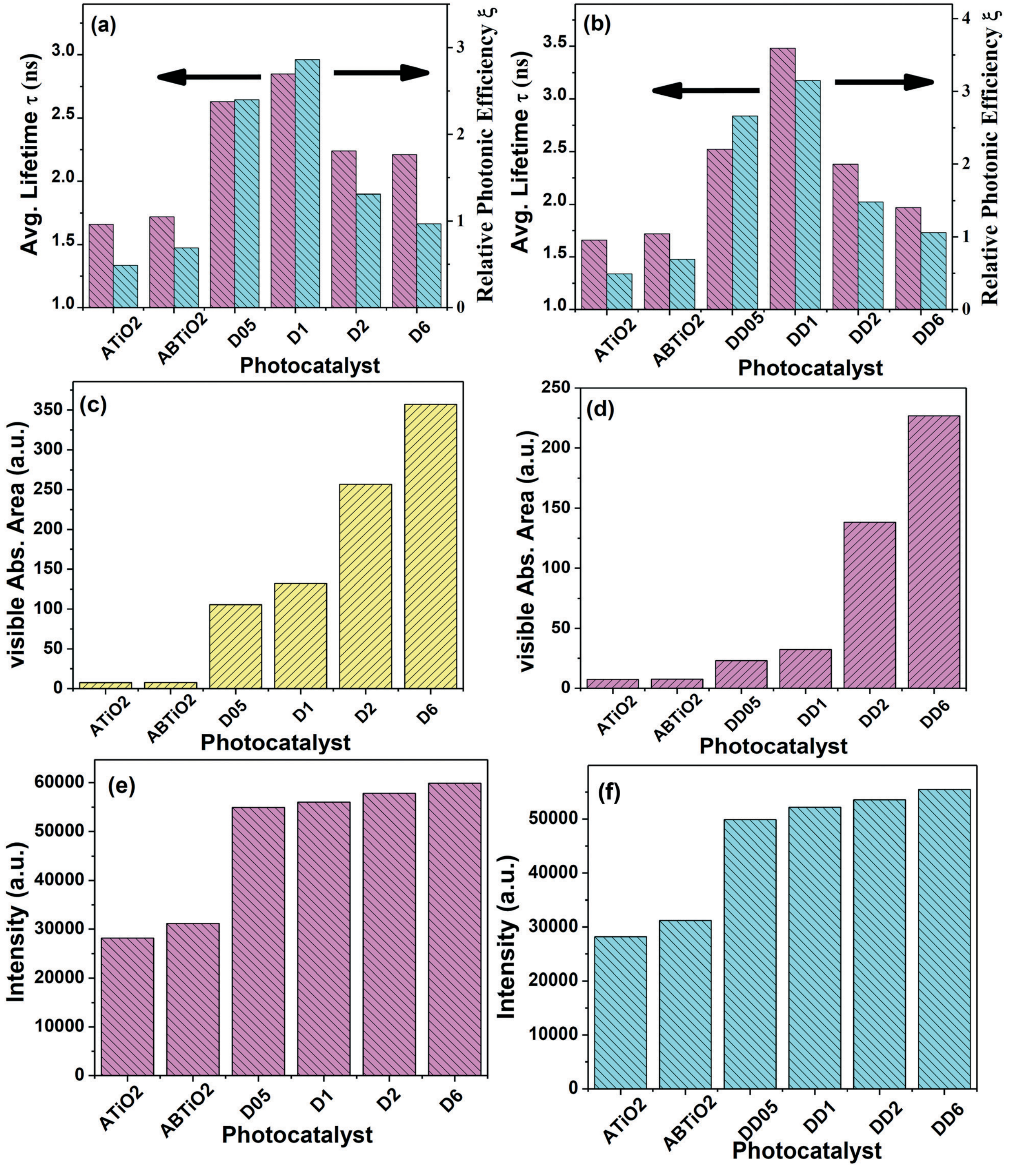

**Fig. 7** (a and b) Variations in the average lifetime and relative photonic efficiency, (c and d) visible absorbtion (400 to 800 nm) area, and (e and f) Raman intensity of Eg mode of the D-ABTiO$_2$ and DD-ABTiO$_2$ powders with different silver concentrations.

methylene blue dye were also determined, as shown in Fig. S6 (ESI‡); similar results were observed.

Analysis of the above data is presented in Fig. 7 for both samples; this clearly shows that the relative photonic efficiency of photocatalytic activity correlates with the average lifetimes of the photogenerated charges and does not correlate with the amount of visible light absorbed, band-gap reduction or plasmonic effects for the Ag–TiO$_2$ system. The details of Fig. 7 are as follows. Fig. 7(a and b) display the average lifetimes of the e–h pairs and the relative photonic efficiencies of photocatalytic activity for all the samples. Fig. 7(c and d) display the amount of visible light absorbed, as calculated from the areas under the curves in the visible range (400 to 700 nm) for all the samples. The presence of the $Ag_{4d}$ level very close to the valance band effectively decreases the band gap in the case of the DD-ABTiO$_2$ sample (doped and decorated). The band gaps calculated from the Tauc plots for various samples (Fig. S7‡) show a decrease as the Ag concentration increases. The Raman signal intensity is enhanced because of the large local electric fields near the surface of Ag NPs, caused by the plasmonic effect. The intensity of the Raman signal is enhanced as the concentration of Ag NPs increases; this can be easily seen in Fig. 1(c and d) and is represented in the histograms in Fig. 7(f and g).

Fig. 8 shows the plot of the relative photonic efficiency of photocatalytic activity *vs.* average lifetime, indicating an almost linear relationship. The question is why, for Ag–TiO$_2$ systems, the photocatalytic activity depends mainly on the lifetimes of photogenerated charges and not on other effects. To answer this question, we propose the following mechanism and explain it based on the schematic displayed in Fig. 9. In Fig. 9, TiO$_2$ is shown schematically as a spherical particle with Ag sitting on it as a decorated Ag NP. The two colors in the TiO$_2$ particle represent the brookite and anatase phases. The small dots in TiO$_2$ are Ag atoms doped in the lattice of TiO$_2$. The relevant energy band diagram is shown inside the particles. Due to the different work functions of TiO$_2$ and Ag, a Schottky barrier 0.3 eV in height is formed (considering TiO$_2$ as n-type semiconductor). Ag doping creates the Ag 4d state near the valence band of TiO$_2$ (for simplicity, this is shown only in the anatase part). The increase in lifetime of ABTiO$_2$ compared to ATiO$_2$ is due to the presence of brookite phase. As shown in Fig. 9, the charges are separated because of the difference in the VBM levels of the brookite and anatase phases.[36]

The interaction between the brookite and anatase NPs causes a facile, irreversible charge transfer from brookite to anatase due to the difference between the band edges of the two phases.[34] This effect reduces the recombination of photogenerated electrons and holes and consequently improves the photocatalytic efficiency of our mixed-phase ABTiO$_2$ samples. The effects of the $Ag_{4d}$ state are to increase visible light absorption and also act as a hole trap. These hole trappings, because of Ag doping, reduce the recombination of mobile charges up to a certain concentration of Ag doping. As the Ag concentration increases, these same traps act as recombination centers, as previously reported in the literature.[37–39] This explains the increase in lifetime at low Ag concentrations and the decrease in lifetime at high Ag concentrations. Also, the higher lifetime and higher photocatalytic activity of DDABTiO$_2$ (doped and decorated) compared to DABTiO$_2$ (only decorated) is explained. The decrease in bandgap (Fig. 7(d)), which allows a higher number of e–h pairs to be created by visible light absorption at a higher Ag doping concentration, is offset by the $Ag_{4d}$ levels, which act as recombination centers.

However, the increase in lifetime from Ag doping is marginal, and the main cause is the charge separation caused by the Schottky barrier. As the Ag decorated on the NPs increases, we expect a greater separation of charges; however, at higher Ag concentrations, we obtain further decreases in lifetime and photocatalytic activity. The culprit is the hot electron ($e^-_{SPR}$) injected in TiO$_2$. This circuitous process affects the charge separation in TiO$_2$ and leads to a negative impact on photocatalytic activity at higher Ag concentrations.[25] It must be noted that the hot electron reaching the Ag surface may also be useful for the redox reaction, as shown in the schematic. It must also be noted that the Schottky barrier height should be optimal, as observed in reference,[39] in which the barrier height offered by Ag (0.3 eV) was not sufficient and that offered by Au (1.3 eV) was too high to transfer the electrons to the metal side. Thus, an Au–Ag alloy was used to obtain an intermediate barrier height.[40]

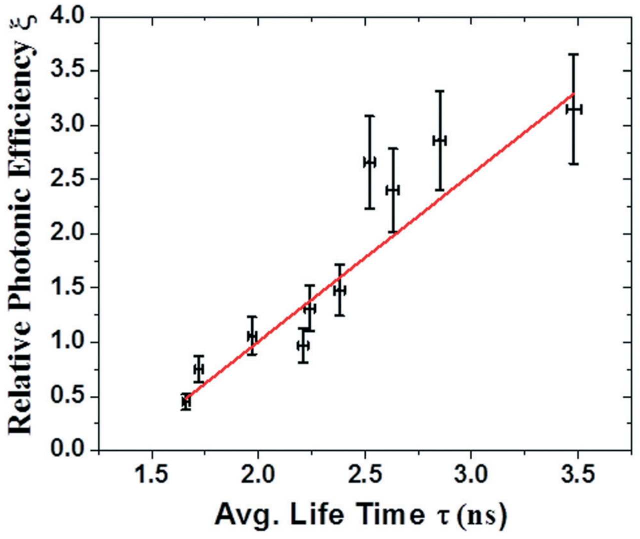

**Fig. 8** Correlation of the photonic efficiencies and average lifetimes of all the photocatalysts prepared in the present work.

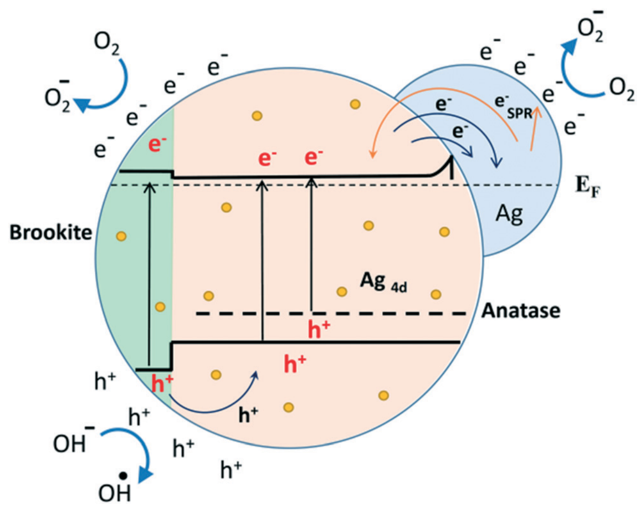

**Fig. 9** Schematic illustrating the photocatalytic degradation of an organic pollutant over the Ag–ABTiO$_2$ photocatalyst under solar light irradiation.

Now, let us consider why the increase in visible light absorption (Fig. 7(c and d)) does not cause an increase in photocatalytic activity. We know that this visible light absorption is caused by the SPR effect and does not cause the creation of e–h pairs in $TiO_2$; therefore, it does not affect the photocatalytic activity. The light harvesting effect of SPR may be marginally helpful. Similarly, thermalization of hot electrons may marginally increase the activity. However, these effects seem to play minor roles compared to the increase in lifetimes of the e–h pairs for the Ag–$TiO_2$ system. However, we observed an increase in the Raman signal as the Ag concentration increased for both samples (Fig. 7(f and g)). Localized surface plasmon resonance (LPSR) mediated field enhancement is thus present; this raises the question of why it does not affect the photocatalytic activity. The answer lies in the model presented by Ingram *et al.*,[41] which states that the SPR spectrum and the absorption spectrum of $TiO_2$ must overlap. In our case, the SPR spectrum is in the visible range, whereas the $TiO_2$ spectrum is marginally extended to the visible range by Ag doping. Therefore, the LPSR-mediated field enhancement will not lead to an increase in the number of e–h pairs. Thus, the key to fully exploit the Schottky effect and the SPR effect is to obtain an optimum barrier height as well as the overlap of the SPR spectrum and the absorption spectrum. Now, the question is whether the increase in lifetime is caused by charge transfer to the silver NPs alone or if there is another mechanism. We obtained some clues from the fast ($\tau_1$) and the slowest ($\tau_3$) measured components of the lifetimes. The fast component is related to recombination of the electron–hole pairs in the conduction and valance bands. These charges are separated by the Schottky barrier. However, the slowest lifetime component ($\tau_3$), which is related to the $Ti^{3+}$ (oxygen vacancy) deep traps, shows a similar trend. This may indicate that the Ag NPs on the surface of $TiO_2$ aid the formation of $Ti^{3+}$ (surface oxygen vacancy), as observed in ref. 42. These centers are electron traps and further aid the redox reaction. This leads us to conclude that for the Ag–$TiO_2$ system, the photocatalytic activity is directly proportional to the photogenerated charge carrier lifetime. There are examples in the literature where no correlation between the light absorption capacity and the rate of photocatalytic degradation was found.[43–44] In fact, a recent review emphasizes that breakthroughs in photocatalysis will occur when the factors that suppress electron–hole recombination are identified.[45]

# Conclusion

We summarize our results as follows. Compared to Ag-decorated samples, Ag-doped and decorated samples show enhanced photocatalytic activity due to the synergistic effects of the Schottky barrier, doping, and anatase + brookite mixed phase. It was observed from PL and lifetime fluorescence studies that the charge carrier lifetimes of the samples correlate with their relative photonic efficiencies of photocatalytic activity. An optimal Ag concentration is required to obtain the maximum lifetime of photo-generated charges. The photocatalytic activity does not show any correlation with the amount of visible light absorption, plasmonic effects, or band-gap reduction. Decorating with silver nanoparticles aids electron transfer and creates electron traps in the form of oxygen vacancies on the surface of $TiO_2$. We show that for the Ag–$TiO_2$ system, the charge separation mechanism is more effective than band-gap reduction or plasmonic effects. To design next-generation photocatalysts, more emphasis must be placed on efficient charge carrier separation and efficient charge transfer to the active sites.

# Acknowledgements

This work was supported by the Department of Science and Technology, New Delhi (India) in the form of a Women Scientists-A (WOS-A) scheme (Sanction no. SR/WOS-A/PS-62/2012) sanctioned to R. S. Varma. R. Fernandes acknowledges UGC for providing financial support through a Dr. D. S. Kothari post-doctoral fellowship.

# References

1 *Environmentally Benign Photocatalysts: Applications of Titanium Oxide-based Materials*, ed. M. Anpo and P. V. Kamat, Springer, 2010.

2 M. Raileanu, M. Crisan, I. Nitoi, A. Ianculescu, P. Oancea, D. Crisan and L. Todan, *Water, Air, Soil Pollut.*, 2013, **224**, 1548.

3 M. Kapilashrami, Y. Zhang, Y. Liu, A. Hagfeldt and J. Guo, *Chem. Rev.*, 2014, **114**, 9662–9707.

4 D. A. Keane, K. G. McGuigan, P. F. Ibanez, M. I. Polo-Lopez, J. A. Byrne, P. S. M. Dunlop, K. O., D. D. Dionysiou and S. C. Pillai, *Catal. Sci. Technol.*, 2014, **4**, 1211–1226.

5 H. Park, H. Kim, G. Moon and W. Choi, *Energy Environ. Sci.*, 2016, **9**, 411–433.

6 A. Bumajdad and M. Madkou, *Phys. Chem. Chem. Phys.*, 2014, **16**, 7146–7158.

7 A. E. Kandjani, Y. M. Sabri, M. Mohammad-Taheri, V. Bansal and S. K. Bhargava, *Environ. Sci. Technol.*, 2015, **49**(3), 1578–1584.

8 M. Pelaez, N. T. Nolan, S. C. Pillai, M. K. Seery, P. Falaras, A. G. Kontos, P. S. M. Dunlop, J. Hamilton, J. Byrne, K. OShea, M. H. Entezari and D. Dionysiou, *Appl. Catal., B*, 2012, **21**, 331–349.

9 J. G. Doh, J. S. Hong, R. Vittal, M. G. Kang, N. Park and K. Kim, *Chem. Mater.*, 2004, **16**, 493–497.

10 L. Li and C. Liu, *Eur. J. Inorg. Chem.*, 2009, **2009**, 3727–3733.

11 Y. Liu, C. Liu, Q. Rong and Z. Zhang, *Appl. Surf. Sci.*, 2003, **220**, 7–11.

12 S. Krejcikova, L. Matejova, K. Koci, L. Obalova, Z. Mataj, L. Capek and O. Solcova, *Appl. Catal., B*, 2012, **111–112**, 119–125.

13 M. Khan, J. Xu, N. Chen, W. Cao, A. Ullah, Z. Usman and D. F. Khan, *Res. Chem. Intermed.*, 2013, **39**(4), 1633–1644.

14 H. Xing-Gang, L. An-Dong, H. Mei-Dong, L. Bin and W. Xiao-Ling, *Chin. Phys. Lett.*, 2009, **26**(7), 077106.

15 N. Sobana, M. Muruganadham and M. Swaminathan, *J. Mol. Catal. A: Chem.*, 2006, **258**, 124–132.

16 H. M. Sung-Suh, J. R. Choi, H. J. Hah, S. M. Koo and Y. C. Bae, *J. Photochem. Photobiol., A*, 2004, **163**, 37–44.

17 S. Anandana, P. S. Kumar, N. Pugazhenthiran, J. Madhavan and P. Maruthamuthu, *Sol. Energy Mater. Sol. Cells*, 2008, **92**, 929–937.

18 G. J. Yang, C. Li, X. Huang, C. Li and Y. Wang, *J. Therm. Spray Technol.*, 2007, **16**(5–6), 881–885.

19 R. Liu, P. Wang, X. Wang, H. Yu and J. Yu, *J. Phys. Chem. C*, 2012, **116**, 17721–17728.

20 P. Christopher, H. Xin and S. Linic, *Nat. Chem.*, 2011, **3**, 467–472.

21 X. Zhang, Y. L. Chen, R. Liu and D. P. Tsai, *Rep. Prog. Phys.*, 2013, **76**, 046401.

22 P. Wang, B. Huang, Y. Dai and M. Whangbo, *Phys. Chem. Chem. Phys.*, 2012, **14**, 9813–9825.

23 K. Ueno and H. Misawa, *J. Photochem. Photobiol., C*, 2013, **15**, 31–52.

24 B. Cojocaru, S. Neatu, E. Sacaliuc-Parvulescu, F. Levy, V. I. Parvulescu and H. Garcia, *Appl. Catal., B*, 2011, **107**, 140–149.

25 M. R. Khan, T. W. Chuan, A. Yousuf, M. N. K. Chowdhury and C. K. Cheng, *Catal. Sci. Technol.*, 2015, **5**, 2522–2531.

26 A. Sclafani and J. M. Hermann, *J. Photochem. Photobiol., A*, 1998, **113**, 181–188.

27 J. M. Buriak, P. V. Kamat and K. S. Schanze, *ACS Appl. Mater. Interfaces*, 2014, **6**, 11815–11816.

28 H. Kisch and D. Bahnemann, *J. Phys. Chem. Lett.*, 2015, **6**, 1907–1910.

29 N. Serpone, G. Sauve, R. Koch, H. Tahiri, P. Pichat, P. Piccinini, E. Pelizzetti and H. Hidaka, *J. Photochem. Photobiol., A*, 1996, **94**, 191–203.

30 N. Serpone, A. Salinaro and IUPAC, *Pure Appl. Chem.*, 1999, **71**, 303–320.

31 K. P. Priyanka, N. A. Sabu, P. A. Sheena, S. Sreeja and T. Varghese, *Adv. Sci., Eng. Med.*, 2014, **6**, 1–5.

32 *Principles of Fluorescence Spectroscopy*, ed. J. R. Lakowicz, Springer, 3rd edn, 2006.

33 F. Cardenas-Lizana, S. Gomez-Quero, H. Idriss and M. A. Keane, *J. Catal.*, 2009, **268**(2), 223–234.

34 N. Daude, C. Gout and C. Jouanin, *Phys. Rev. B: Solid State*, 1977, **15**(6), 3229–3235.

35 A. L. Linsebigler, G. Lu and J. T. Yates, *Chem. Rev.*, 1995, **95**, 735–758.

36 A. D. Paola, M. Bellardita and L. Palmisano, *Catalysts*, 2013, **3**, 36–73.

37 M. Ni, M. K. H. Leung, D. Y. C. Leung and K. Sumathy, *Renewable Sustainable Energy Rev.*, 2007, **11**, 401–425.

38 A. E. Kandjani, M. Mohammadtaheri, A. Thakkar, S. K. Bhargava and V. Bansal, *J. Colloid Interface Sci.*, 2014, **436**, 251–257.

39 R. Dholam, N. Patel, M. Adami and A. Miotello, *Int. J. Hydrogen Energy*, 2009, **34**, 5337–5346.

40 D. Tsukamoto, A. Shiro, Y. Shiraishi, Y. Sugano, S. Ichikawa, S. Tanaka and T. Hirai, *ACS Catal.*, 2012, **2**, 599–603.

41 D. B. Ingram, P. Christopher, J. L. Bauer and S. Linic, *ACS Catal.*, 2011, **1**, 1441–1447.

42 S. X. Liu, Z. P. Qu, X. W. Han and C. L. Sun, *Catal. Today*, 2004, **93–95**, 877–884.

43 K. Nagveni, M. S. Hegde and G. Madras, *J. Phys. Chem. B*, 2004, **108**, 20204–20212.

44 N. Patel, A. Dashora, R. Jaiswal, R. Fernandes, M. Yadav, D. C. Kothari, B. L. Ahuja and A. Miotello, *J. Phys. Chem. C*, 2015, **119**, 18581–18590.

45 B. Ohtani, *Catalysts*, 2013, **3**, 942–953.